Publications of the Astronomical Society of the Pacific, 132:034502 (18pp), 2020 March https://doi.org/10.1088/1538-3873/ab694d

Sixteen Open Clusters Discovered with Sample-based Clustering Search of *Gaia* DR2

ChaoJie Hao[1,2], Ye Xu[1], ZhenYu Wu[3,4], ZhiHong He[1,2], and ShuaiBo Bian[1,2]
[1] Purple Mountain Observatory, Chinese Academy of Sciences, Nanjing 210023, People's Republic of China; cjhao@pmo.ac.cn, xuye@pmo.ac.cn
[2] School of Astronomy and Space Science, University of Science and Technology of China, Hefei 230026, People's Republic of China
[3] Key Laboratory of Optical Astronomy, National Astronomical Observatories, Chinese Academy of Sciences, Beijing 100012, People's Republic of China
[4] School of Astronomy and Space Science, University of Chinese Academy of Sciences, Beijing 101408, People's Republic of China
Received 2019 November 25; accepted 2020 January 8; published 2020 February 4

Abstract

Accurate astrometric parameters and photometric data in three bands for more than 1.3 billion sources (mainly stars) were made available in the recent *Gaia* Data Release 2, allowing us to find new open clusters in the milky Way. We propose a novel sample-based clustering search method with high spatial resolution to search for open clusters (OCs). We used the proposed method to find 16 new OC candidates. Their astrometric parameters are presented, including age, etc.

Key words: methods: data analysis – methods: statistical – open clusters and associations: general

Online material: color figures

1. Introduction

An open cluster (OC) is a stellar group of up to a few thousand stars. These stars form simultaneously in a giant molecular cloud (Lada et al. 1993) such that they are roughly the same age and bounded by mutual gravitational attraction. OCs have been found only in spiral and irregular galaxies, in which active star formation is occurring (Payne-Gaposchkin 1979). Young OCs are effective tracers for the structure and evolution of the Milky Way (Janes & Adler 1982; Dias & Lépine 2005; Piskunov et al. 2006; Moitinho 2010). It was believed that the census of the population of OCs was complete up to distances of 1.8 kpc (Alessi et al. 2003; Kharchenko et al. 2005; Röser et al. 2016). However, recent studies have supported the doubts expressed by Moitinho (2010) on the claim of completeness (Cantat-Gaudin et al. 2018a, 2018b; Castro-Ginard et al. 2018, 2019; Liu & Pang 2019; Sim et al. 2019).

The recent *Gaia* Data Release 2 (Gaia DR2) includes accurate astrometric parameters (position, parallax, and proper motions) for more than 1.3 billion sources (mainly stars), including three-band photometry (Gaia Collaboration et al. 2018). This enormous database opens a new era for the study of OCs in the Milky Way. Castro-Ginard et al. (2018) developed an OC search method using an algorithm called the density-based spatial clustering of applications with noise (DBSCAN) (see Section 2.2, Ester et al. 1996) and detected 31 new OC candidates. They confirmed that DBSCAN can reliably detect OCs using the *TGAS* data set (Tycho *Gaia* Astrometric Solution, Michalik et al. 2015; Lindegren et al. 2016) and *Gaia* DR2. They explored the Milky Way disk by scanning all longitudes in the region $\pm 20^\circ$ in latitude. They also detected 53 OCs that were previously unknown in a region covering the Galactic anticentre and the Perseus arm ($120^\circ \leqslant l \leqslant 205^\circ$ and $-10^\circ \leqslant b \leqslant 10^\circ$) using the same method (Castro-Ginard et al. 2019).

Cantat-Gaudin et al. (2018a) detected 54 new objects by applying the membership assignment code, UPMASK (Unsupervised Membership Assignment Method in Stellar Clusters, Krone-Martins & Moitinho 2014) to stellar fields centered on each known cluster or candidate. They compiled a list of 3328 known clusters and candidates taken from the catalogs of Dias et al. (2002) and Kharchenko et al. (2013), and the publications of Froebrich et al. (2007), Schmeja et al. (2014), Scholz et al. (2015), and Röser et al. (2016). They relied exclusively on *Gaia* DR2 and applied UPMASK to determine lists of OC member stars. They also reported the discovery of 41 new candidates in the direction of Perseus (Cantat-Gaudin et al. 2018b), using a variant of the method. They used data from the entire region defined by galactic coordinates $l \in [120^\circ, 200^\circ]$ and $b \in [-10^\circ, 10^\circ]$.

In this study, we propose a new method that improves the efficiency of detection as well as the quality of member stars. The UPMASK used by Cantat-Gaudin et al. (2018a) provided member stars and mean parameters for a set of 1212 OCs and 54 newly discovered objects. With their method, however, only small groups of stars were identified in the three-dimensional astrometric space (ϖ, $\mu\alpha^*$, $\mu\delta$). The total number of clusters for which they were able to identify members (1212) was significantly lower than the initial list of clusters and candidates (3328).

Our proposed method, the sample-based clustering search method (SBCSM), employs the DBSCAN algorithm (Castro-Ginard et al. 2018). However, we selected a much smaller region, which is more sensitive to cluster density. Our proposed method discovered 16 new OC candidates.

2. Method

2.1. Sample Selection

The parameters of the DBSCAN algorithm are based on big regions—more than one hundred square degrees. Yet DBSCAN is a density-based clustering algorithm, and background field stars have a great impact on star clusters, such that large regions can result in missed objects. Therefore, the regions we selected were smaller than before. As such, we can improve the spatial resolution to discover more objects. The efficiency of detection for OCs is closely related to the extent and distance of the region. Hence, as we narrowed the region and analyzed the search results, we found that tiles of $1^\circ \times 1^\circ$ were ultimately the best. Larger regions (such as $2^\circ \times 2^\circ$, $3^\circ \times 3^\circ$, etc.) incur more time for calculations. More importantly, some targets are left out (almost 30%). Distributions are more extended for closer targets, so smaller ranges (such as $0.^\circ5 \times 0.^\circ5$, etc.) result in missed memberships. Therefore, the tiles of $1^\circ \times 1^\circ$ offer the spatial resolution needed to best unveil OCs. In particular, if the amount of data for exceptive areas is extremely large, the sources in these areas can be layered according to the parallax (usually divided into two layers).

Thus, smaller regions reduce the computational time, and insofar as the DBSCAN (see Section 2.2, Ester et al. 1996) algorithm requires a starting source to define the average density of sources in the region, smaller regions are more representative than the entire sky. Furthermore, the subsequent parameters obtained in small tiles are more efficient. However, when the sky is divided into small tiles, targets can be located at the edges of areas. To solve this problem, the right ascension (R.A.) and declination (decl.) can be translated up and down and to the right and left. Thus, clustering analysis can be performed multiple times.

2.2. Spatial Clustering Algorithm: DBSCAN

We mainly used the proposed SBCSM to generate suitable parameters for the DBSCAN algorithm (Ester et al. 1996). DBSCAN is a density-based algorithm that uses the concept of the distance between two sources to define a set of nearby points as clusters. It offers advantages over other methods that can find clusters of arbitrary shapes.

DBSCAN describes the proximity of a sample based on a set of neighborhoods. The definition of a cluster depends on two parameters: ϵ and *minPts*. They are used to describe the proximity of the sample distribution in the neighborhoods, where ϵ describes the neighborhood distance threshold of the sample, and *minPts* describes the number of objects in the sample neighborhoods with distance ϵ.

A hypersphere with a radius ϵ is centered on each source. If the number of sources falling within the hypersphere is greater than or equal to the preset *minPts*, then these objects are considered to be clustered. Consequently, the types of sources in space can be divided into three types:

Core object: A source with multiple "neighbors" greater than or equal to *minPts* (within the hypersphere of radius ϵ).

Member objects: There are no or few sources in their hyperspheres but they are within the hypersphere of a core object.

Noise object: A source that does not correspond to the first two conditions.

The clustering results are completely reliant on the parameters ϵ and *minPts* that we set. When the parameter values ϵ and *minPts* are too large, we will find many clusters. By contrast, when the parameters are too small, none will be found and all sources will be considered noise. In addition, we found that the influence of the parameter ϵ is more significant to the clustering results. For the DBSCAN algorithm, it is indispensable to determine suitable parameters.

2.3. Statistical Analysis

Before searching for OCs, we analyzed the parametric characteristics of a large number of known clusters and candidates. This step is significant to the DBSCAN algorithm, with which we can estimate whether the indicators of *N*-dimensions are balanced. Member stars of OCs are clusters with common origins, with a similar position (R.A., decl., ϖ) and proper motion ($\mu\alpha^*$, $\mu\delta$). Therefore, the parameters of these five-dimensions can be used as the foundation for the search for OCs. We performed statistical analysis on 1229 known OCs as well as candidates to confirm the efficiency of SBCSM, based on the work in Cantat-Gaudin et al. (2018a). We extracted the position, parallax, and proper motion of member stars from these 1229 clusters and candidates. Then, we calculated the information entropy and entropy weight of these five indicators in each sample separately, using the entropy weight method (EWM) (EWM, Kemal & Yakup 2018).

The principle of the EWM is to determine the objective weight based on the magnitude of the variability of the index. Entropy is the measure of uncertainty, and this can be used to determine the degree of dispersion of an indicator. If the degree of dispersion of an indicator is higher, the entropy value will be smaller, and the index will have more influence on the comprehensive evaluation. The EWM proceeds in three steps: standardizing data, finding the information entropy of each indicator, and determining the entropy weight of each indicator.

Figure 1 presents the information entropy and entropy weights for these five indicators. It can be elicited that the

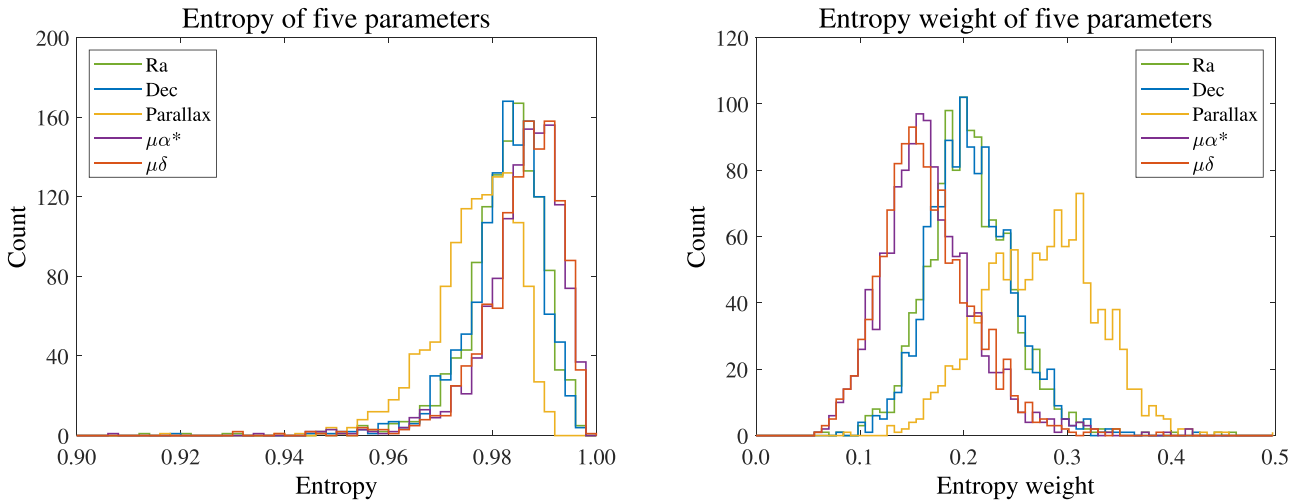

Figure 1. Information entropy (left) and entropy weight (right) of the five-dimensional parameters of 1229 clusters and candidates. The different colors represent five different indicators: green, blue, yellow, purple, and brown represent the R.A., decl., parallax, proper motion $\mu\alpha^*$, and proper motion $\mu\delta$.
(A color version of this figure is available in the online journal.)

distribution of each entropy value and entropy weight of these five parameters is basically semblable. The entropy of the parallax is minimal, and the R.A. and decl. take second place. It is clear that the entropy weight of the parallax is larger than the position (R.A., decl.) as well as the proper motion. The size and shape of the OCs are particularly uncertain, but the proper motions are so similar that the dispersion is extremely small.

Although the positions (R.A., decl.) of the member stars are similar, it is impossible for them to be distributed in the same location. Likewise, the parallax also has a higher degree of dispersion. Therefore, these five indicators are distribution features that are completely rational and acceptable. This further indicates that the OCs are authentically irregular. On the other hand, we can conclude that the dispersion of these five indicators is approximately uniform, such that there is no need to weigh the indicators specifically for the DBSCAN algorithm, which assigns equal weight to these five parameters.

2.4. Data Normalization

The units of data in *Gaia* DR2 differ in position, parallax, and proper motion. It is thus inconvenient to perform statistical analysis directly. In order to eliminate the discrepancy of the units as well as the range difference between the indicators, which will significantly influence the results of clustering analysis, the data needs to be standardized. That is, the data must be scaled proportionally to fall into a specific area. It will be advantageous to do so before proceeding to the comprehensive analysis. There are two main methods of standardizing data:

Min–max standardization: Linear normalization, or dispersion normalization, involves a linear transformation of the original data that causes the results to fall within the [0,1] interval. The conversion function is as follows:

$$x^* = \frac{x - \min}{\max - \min}. \tag{1}$$

For this method, max is the maximum value of the sample data, and min is the minimum value. Hence, this normalization method is more suitable for cases where the numerical comparison is concentrated. However, the method has a drawback. If the maximum and minimum are unstable, the normalization results can be precarious. Moreover, the maximum and minimum values will change when new data is added, at which point they will need to be redefined. Consequently, empirical constants can be used to replace the maximum and the minimum. In practice, we have found that this normalization method has distinct drawbacks for the data from *Gaia* DR2.

z-score standardization: This standardization method is based on the mean and standard deviation of the data from the sample, where the original value x of the sample A is normalized to x'. z-score normalization is exceptionally applicable to the case where the maximum and minimum values of the sample A are unknown, or when out-of-group data exceeds the value range. By using this transformation, all data for each attribute is eventually aggregated with a mean of 0 and a variance of 1. The conversion function is as follows:

$$x^* = \frac{x - \mu}{\sigma}. \tag{2}$$

We found that this normalization works better in practice. Actually, z-score standardization performs better when the distance is used to measure the similarity, especially in classification and clustering algorithms. This is because the dimension of each dimension is equivalent when using it.

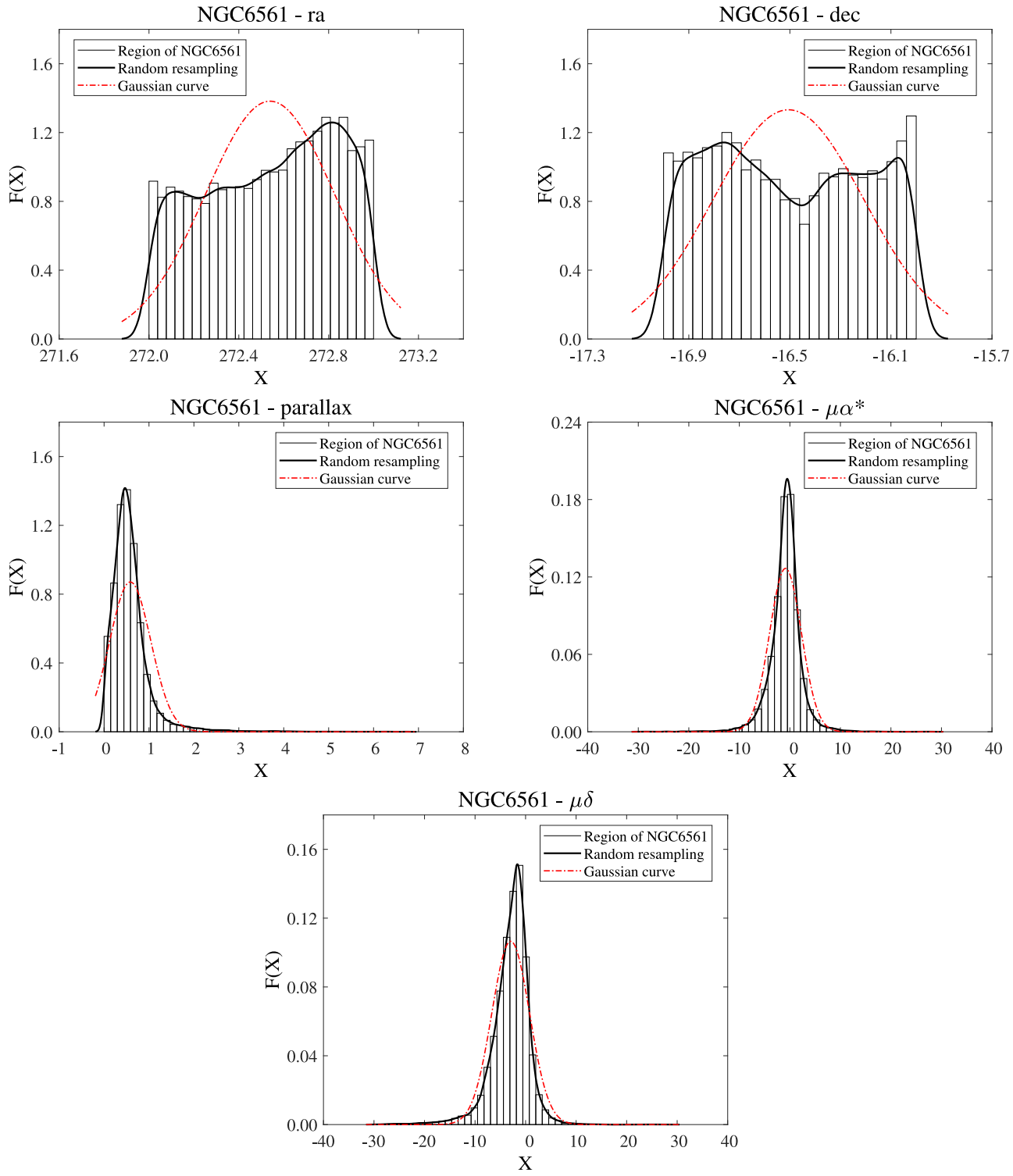

Figure 2. Histogram of the data distribution of the region around cluster NGC 6561. The solid black line is the distribution curve of the generated random sample. The red dotted line shows a normal distribution, which is the fitting curve of the observed region itself (where the mean and variance are derived from the region around this cluster). X is the actual value of the parameter of the observed sample, and $F(x)$ is obtained from the probability density function.
(A color version of this figure is available in the online journal.)

Table 1
Summary of 34 Known Open Clusters and Candidates Found with the Proposed SBCSM

Trumpler_14	Dias_6	NGC 581	NGC 6561	Berkeley_30	Ruprecht_18	Alessi_Teutsch_8	Alessi_10	FSR_1363
Trumpler_15	IC_4996	NGC 1893	NGC 7031	Berkeley_33	Ruprecht_63	Majaess 211	NGC4103	Dolidze_53
Trumpler_16	Pismis_3	NGC 2254	NGC 7654	Berkeley_69	Ruprecht_172	Feibelman_1	Berkeley_86	Dolidze_20
Alessi_12	Teutsch_7	NGC 3532	LDN_988e	Berkeley_85	Barkhatova_1	UBC67		

Note. Lists: Kharchenko et al. (2013), Dias et al. (2014), Cantat-Gaudin et al. (2018a), Castro-Ginard et al. (2019).

The process of data normalization involves scaling the stellar parameters used by the subsequent DBSCAN algorithm, because the algorithm uses the distance between the sources in the N-dimensional space to define whether the stars are aggregated. And we have found that the weights of these five parameters (R.A., decl., ϖ, $\mu\alpha^*$, and $\mu\delta$) are equivalent. For this reason, we used z-score normalization.

2.5. Gaussian Kernel Density Estimation (GKDE)

We generated random samples for each small tile with the same number and distribution of the five astrometric parameters (R.A., decl., ϖ, $\mu\alpha^*$, and $\mu\delta$). The random samples obtained by GKDE will affect the parameter settings for the DBSCAN clustering algorithm, with which we can reduce parametric errors from the instability of the distribution of the observed sample. In other words, the random sample greatly improves the accuracy of the algorithm parameters that we set. In our evaluation, we could find only half of the objects when we omitted this process.

The principle of the kernel density function (Zambom & Dias 1998) is relatively straightforward. If we know the probability distribution of an object in advance, and if there is a determinate amount in the observation, we can consider that the probability density of this object is very large. Moreover, the density will be even higher when the probability is adjacent to this object. By contrast, if the probability is away from this object, the density will be smaller.

Kernel density estimation (KDE, Lampe & Hauser 2011) is used in probability theory to estimate the density function of variables. It is one of the non-parametric tests. We used the GKDE to generate a new random sample with the same number of stars as the observed sample. Furthermore, we used the five random astrometric parameters (R.A., decl., ϖ, $\mu\alpha^*$, and $\mu\delta$) according to the distribution of the primordial sample (Castro-Ginard et al. 2018).

Based on this idea, we can use a kernel function (K) to fit the farthest and most recent probability density for each object in the observed sample. Subsequently, a plurality of probability density distribution functions fitted to each of the observed objects is averaged. If there are some important objects, they can be processed using a weighted average. Notably, we are not trying to find the true distribution function. The essence of KDE is to use a kernel function (such as a Gaussian function) to obtain the N-kernels function, in which we use the value and bandwidth of each object as the parameters of this function. Then, we use linear superimposition to form a function, and, after normalization, the kernel density can be estimated by it. Moreover, we can use this function to generate a new random sample.

We used a Gaussian kernel for density estimation:

$$K(\|x - xc\|) = \exp\{-\|x - xc\|^{\frac{2}{2\sigma^2}}\}. \quad (3)$$

Here, xc is the center of the kernel function, and σ is the width parameter for the function. The only parameter that needs to be determined is the bandwidth, which is also the standard deviation of the normal distribution.

There are several ways to set the bandwidth h. In this paper, we use the optimal bandwidth based on the characteristics of the sample:

$$h = 1.06 * (\text{std}) * (N_{\text{total}})^{-\frac{1}{5}}. \quad (4)$$

Here, std denotes the sample standard deviation, and N_{total} is the total number of samples. The distribution of random samples generated by setting this bandwidth is consistent with the observed sample.

Figure 2 shows the five parameters (R.A., decl., ϖ, $\mu\alpha^*$, and $\mu\delta$) between the random sample obtained by GKDE and the observed sample of the region around the cluster NGC 6561. The histogram is the distribution of the observed sample, and the solid black curve is the distribution of the random sample. For comparison, the red dotted curve is a normal distribution, which fits the observed sample itself (with the mean and variance derived from the observed sample). It is clear that the black solid curve is consistent with the distribution of the histogram, such that the random sample obtained is indeed credible. In what follows, we show how this random sample is used to generate applicable parameters for the algorithm applied.

2.6. Parameter Determination

DBSCAN can solve the clustering of an irregular shape, while also processing for noise objects. Hence, this algorithm is adaptive to OCs insofar as there are clusters of stars with approximate positions (R.A., decl., ϖ) and proper motions ($\mu\alpha^*$, $\mu\delta$). *Gaia* DR2 contains precise information about these five parameters. In this study, we defined the Euclidean distance between two sources.

Table 2
Summary of Mean Parameters for 16 New OC Candidates

Cluster	R.A. (deg)	Decl. (deg)	R (deg)	N	$\mu\alpha^*$ (mas yr^{-1})	$\mu\delta$ (mas yr^{-1})	ϖ (mas)	d (pc)	A_G	log(age)
OC-1	51.78(0.01)	45.14(0.01)	0.09	43	0.18(0.16)	−2.46(0.17)	0.61(0.01)	1645.3(13.7)	0.70	9.08
OC-2	80.11(0.01)	33.26(0.01)	0.08	32	1.27(0.09)	−3.33(0.12)	0.59(0.01)	1690.9(13.6)	0.80	8.90
OC-3	80.14(0.01)	33.41(0.01)	0.08	24	0.61(0.35)	−5.06(0.35)	1.13(0.02)	882.9(9.2)	0.66	8.90
OC-4	80.25(0.01)	33.83(0.01)	0.06	21	0.55(0.13)	−3.60(0.10)	0.56(0.01)	1762.1(22.4)	1.04	8.76
OC-5	80.37(0.01)	33.39(0.01)	0.05	20	−0.12(0.09)	−3.18(0.08)	0.79(0.02)	1266.8(11.8)	0.88	7.74
OC-6	80.54(0.02)	33.83(0.02)	0.07	15	−0.45(0.16)	−3.43(0.29)	1.27(0.05)	790.2(5.1)	0.90	7.92
OC-7	80.57(0.01)	35.42(0.02)	0.09	19	1.49(0.12)	−2.88(0.23)	0.58(0.02)	1735.0(15.9)	1.18	7.60
OC-8	80.57(0.01)	33.79(0.01)	0.04	21	−0.16(0.06)	−3.13(0.08)	0.85(0.02)	1178.0(9.9)	1.14	7.24
OC-9	80.78(0.02)	33.09(0.01)	0.09	18	1.72(0.29)	−5.15(0.24)	1.15(0.02)	868.5(9.8)	0.64	8.90
OC-10	81.94(0.01)	33.28(0.01)	0.04	18	1.32(0.05)	−2.93(0.05)	0.32(0.01)	3092.5(18.9)	1.28	8.50
OC-11	127.86(0.01)	−47.99(0.01)	0.07	34	−4.34(0.07)	4.61(0.15)	0.57(0.01)	1751.9(17.2)	0.80	8.74
OC-12	167.12(0.01)	−58.74(0.01)	0.09	62	−7.03(0.12)	2.07(0.08)	0.60(0.01)	1655.3(14.6)	0.52	8.84
OC-13	274.21(0.02)	10.79(0.03)	0.17	45	−0.61(0.19)	−6.19(0.24)	1.12(0.01)	890.9(11.2)	0.22	9.60
OC-14	302.38(0.01)	38.29(0.01)	0.03	53	−2.61(0.02)	−4.89(0.02)	0.27(0.01)	3669.9(28.2)	2.66	6.96
OC-15	317.62(0.01)	46.81(0.01)	0.08	134	−3.31(0.01)	−3.63(0.01)	0.14(0.01)	7294.2(25.5)	3.14	6.84
OC-16	318.35(0.01)	46.29(0.01)	0.11	150	−2.59(0.08)	−3.79(0.09)	0.62(0.01)	1611.8(10.6)	1.02	8.58

Note. The parameters shown are the mean and standard deviation for the (N) members found. R: radius containing half the memberships discovered in this study. N: number of member stars. AG: extinction in the G band.

To obtain suitable parameters, we adopted the k-nearest neighbors algorithm (KNN, Altman 1992). To determine the k-value of the kth nearest distance, Castro-Ginard et al. (2018) demonstrated that the result is more effective for OCs when k is [5, 6, 7, 8, 9].

Therefore, we first calculate the distance sets of the sources after normalization of the observed samples, which means calculating the distance between all sources in the $m* n$-dimensional matrix. After sorting the distance, we extract the 5th, 6th, 7th, 8th, and 9th distance sets for the observed samples as follows: $E'(5)$, $E'(6)$, $E'(7)$, $E'(8)$, and $E'(9)$, respectively. Ultimately, we take the minimum of each set as follows: $\epsilon_{\text{obs-5}}$, $\epsilon_{\text{obs-6}}$, $\epsilon_{\text{obs-7}}$, $\epsilon_{\text{obs-8}}$, and $\epsilon_{\text{obs-9}}$, respectively. Similarly, for the random samples generated by GKDE, as with the observed samples, ϵ denotes $\epsilon_{\text{rand-5}}$, $\epsilon_{\text{rand-6}}$, $\epsilon_{\text{rand-7}}$, $\epsilon_{\text{rand-8}}$, and $\epsilon_{\text{rand-9}}$, respectively.

In order to obtain the concentrated clusters and minimize the pollution effect of field stars, our choice for the distance parameter ϵ is $\epsilon = (\epsilon_{\text{obs}} + \epsilon_{\text{rand}})/2$. Since *minPts* determines the minimum number of members in the cluster, the relationship between the k and *minPts* is $k = minPts - 1$. Therefore, ϵ has a one-to-one correspondence with *minPts*.

3. Data

To demonstrate the superiority of the proposed SBCSM, we took the mean parameters of R.A. and decl. for each OC candidate as the center points. These were taken from the 54 new OC candidates discovered by Cantat-Gaudin et al. (2018a). Then, the small tiles were set to the squares of $1^\circ \times 1^\circ$ in these center points to derive all sources in these areas. The data was collected from the *Gaia* data website of the ESA: https://gea.esac.esa.int/archive/.

We rejected sources with abnormal proper motion and parallax, such as particularly large or negative parallax or extremely large motion. The rejection criterion was set as follows: $|\mu\alpha^*|, |\mu\delta| > 30$ mas yr^{-1}; $\varpi < 0$ mas and $\varpi > 7$ mas; $G > 18$. Cantat-Gaudin et al. (2018a) concluded the characteristics of sources in *Gaia* DR2: stars with a magnitude greater than 18 (weaker stars) have particularly large parallax errors, even exceeding 0.2 mas. As Cantat-Gaudin et al. (2018a) did, we made use of sources that brighter than $G = 18$, corresponding to typical astrometric uncertainties of 0.3 mas yr^{-1} in proper motion and 0.15 mas in parallax, and the individual errors of the sources were not taken into account in the proposed method.

4. Results

In total, we found 104 OCs and OC candidates. These 104 objects have been cross-matched with known catalogs of OCs (Kharchenko et al. 2013; Dias et al. 2014; Cantat-Gaudin et al. 2018a; Castro-Ginard et al. 2019), including position (R.A., decl.), parallax and proper motion. The criterion in three parameter spaces was set as follows: distance between the centers of two clusters is 3 times greater than the sum of the radii of two clusters; difference of mean parallax between two clusters is 5 times larger than the standard deviation; the criterion of proper motion is the same as parallax. We confirmed all 54 OC candidates that were previously discovered by Cantat-Gaudin et al. (2018a), with 100% efficiency. Furthermore, 34 other known OCs and candidates were discovered (see Table 1). Among these 34 known OCs

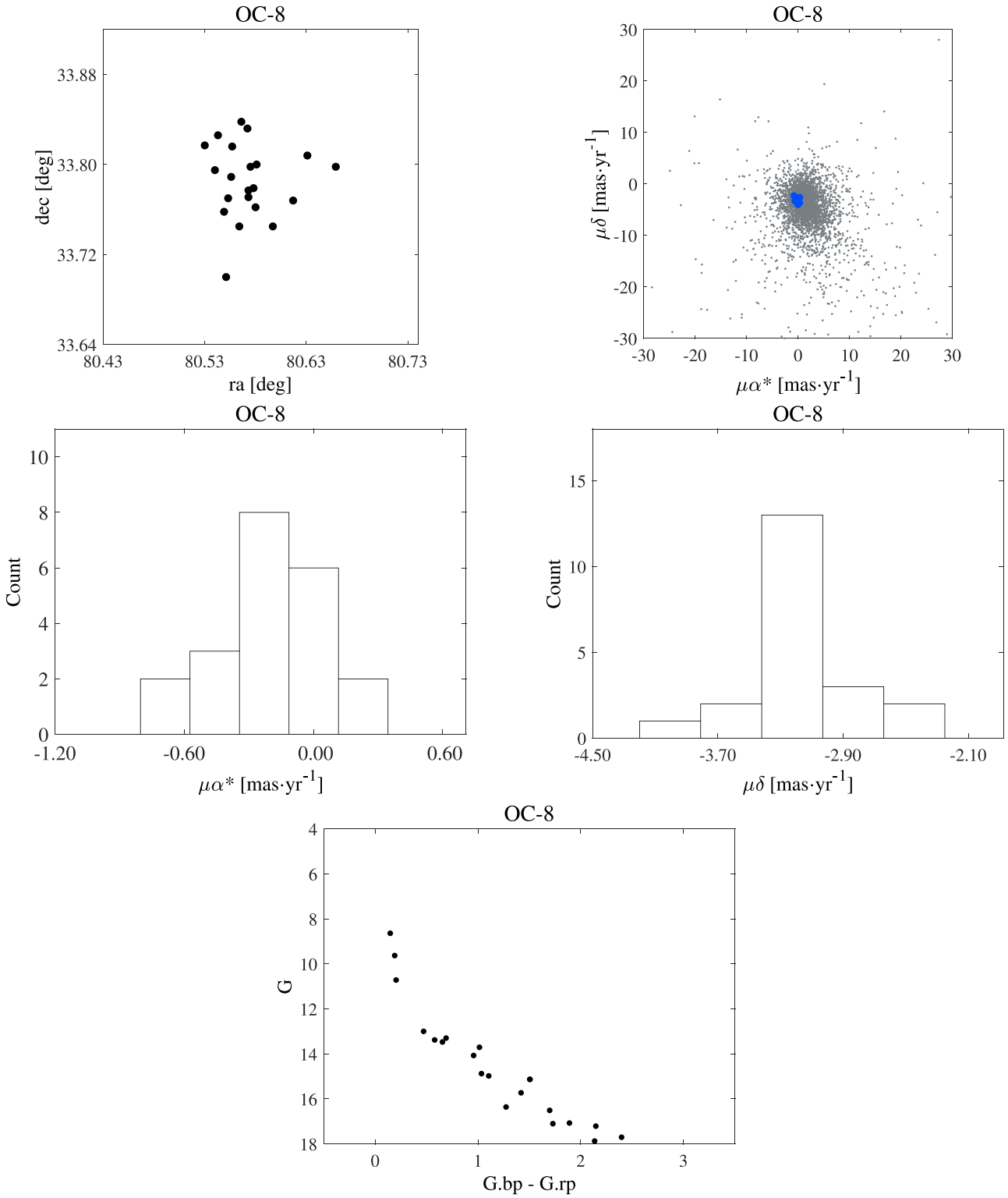

Figure 3. Top left: member stars (black) in the sky for OC-8 (R.A., decl.). Top right: member stars (blue) together with field stars (gray) for OC-8 in proper motion space. Middle: histograms of proper motion. Bottom: color–magnitude diagram showing the sequence of the members.
(A color version of this figure is available in the online journal.)

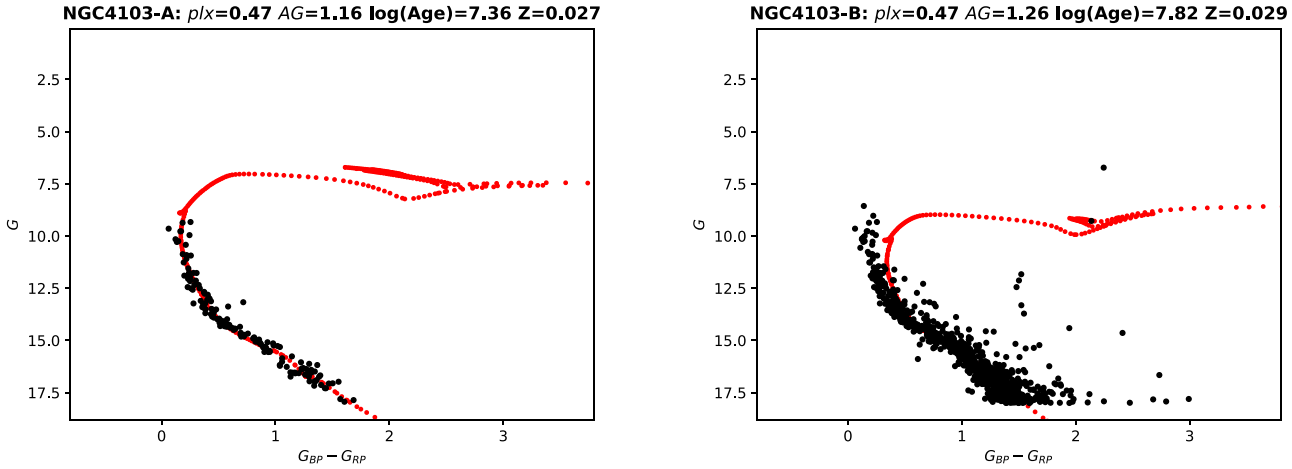

Figure 4. CMDs for a sample of NGC 4031 from this work (left) and from Cantat-Gaudin et al. (right). The red curves denote theoretical isochrones corresponding to the cluster parameters.

(A color version of this figure is available in the online journal.)

and candidates, 31 were noted by Cantat-Gaudin et al. (2018a) and the remaining 3 objects were found by other projects. We confirmed the OCs Dolidze_20 and LDN_988e (Kharchenko et al. 2013; Dias et al. 2014). We also confirmed the OC candidate UBC67, which was recently discovered by Castro-Ginard et al. (2019). Beyond this, 16 new OC candidates were obtained in these areas. None of these 16 new candidates is compatible in at least one parameter space (see Figure 7). Evidently, the SBCSM offers very high spatial resolution for unveiling OCs, along with good accuracy.

4.1. New OC Candidates

Table 2 lists the parameters of the 16 new OC candidates. We calculated the mean position (R.A., decl.), parallax, and proper motion of each candidate, including the standard deviation. These new candidates were obtained using the proposed SBCSM.

Figure 3 shows the distribution in the sky of a new OC candidate, OC-8, along with the proper motion of member stars and the distribution characteristics of the color–magnitude diagrams (CMDs). The candidate OC-8 is distributed on $80^{\circ}.57$ (R.A.) and $33^{\circ}.79$ (decl.), with a radius of about $0^{\circ}.04$. Its distance is about 1.2 kpc, with proper motion of -0.16 and -3.13 mas yr^{-1}. This is the radius containing half of the member stars discovered in this work, and the distance of each OC candidate is the mode of the distance likelihood.

4.2. Age Determination

OCs are considered to be groups of stars with common origins and with similar position and proper motion (R.A., decl., ϖ, $\mu\alpha^{*}$, $\mu\delta$). Member stars are formed almost simultaneously in a giant molecular cloud and are roughly the same age. Therefore, the CMDs can provide empirical isochrones for comparison with theoretical models (Castro-Ginard et al. 2018). The distribution of the member stars of an OC is almost concentrated on a theoretical curve.

To estimate the cluster age, we constructed CMDs for our OC candidates. We compared each CMD to the metallicity $z = 0.015$–0.029 isochrones of the PARSEC library (Bressan et al. 2012), updated for the *Gaia* DR2 passbands with photometric calibration of Evans et al. (2018). The least-squares fitting of isochrones was used to match the observed cluster CMDs. We used the inverse of the averaged parallax as the cluster distance. The CMDs were corrected for the extinction AG and reddening E (G_{BP}–G_{RP}), using the extinction law $R_v = 3.1$ (Cardelli et al. 1989; O'Donnell 1994). We selected those candidate clusters with CMDs that (visually) appeared well-fitted to theoretical isochrones and estimated their age. The results are shown in Table 2.

Figure 4 shows the results of theoretical curves that fit NGC4103. The parameters that come from this theoretical curve are shown at the top of the figure. We compared the member stars we obtained with Cantat-Gaudin et al. (2018a). It can be clearly seen that the memberships we obtained are strongly distributed on a theoretical curve and have higher goodness of fit. The memberships from Cantat-Gaudin's project Cantat-Gaudin et al. (2018a) have high dispersion, and there are some member stars that deviate significantly from the theoretical curve. Furthermore, it is extremely difficult to find a theoretical curve fitted to member stars from Cantat-Gaudin et al. (2018a) because there are many memberships that cannot be on a curve in the meantime.

5. Discussion

We compared the OC candidate Gulliver18 obtained by SBCSM to that found by Cantat-Gaudin et al. (2018a). Figure 5 distinguishes these two candidates and includes their

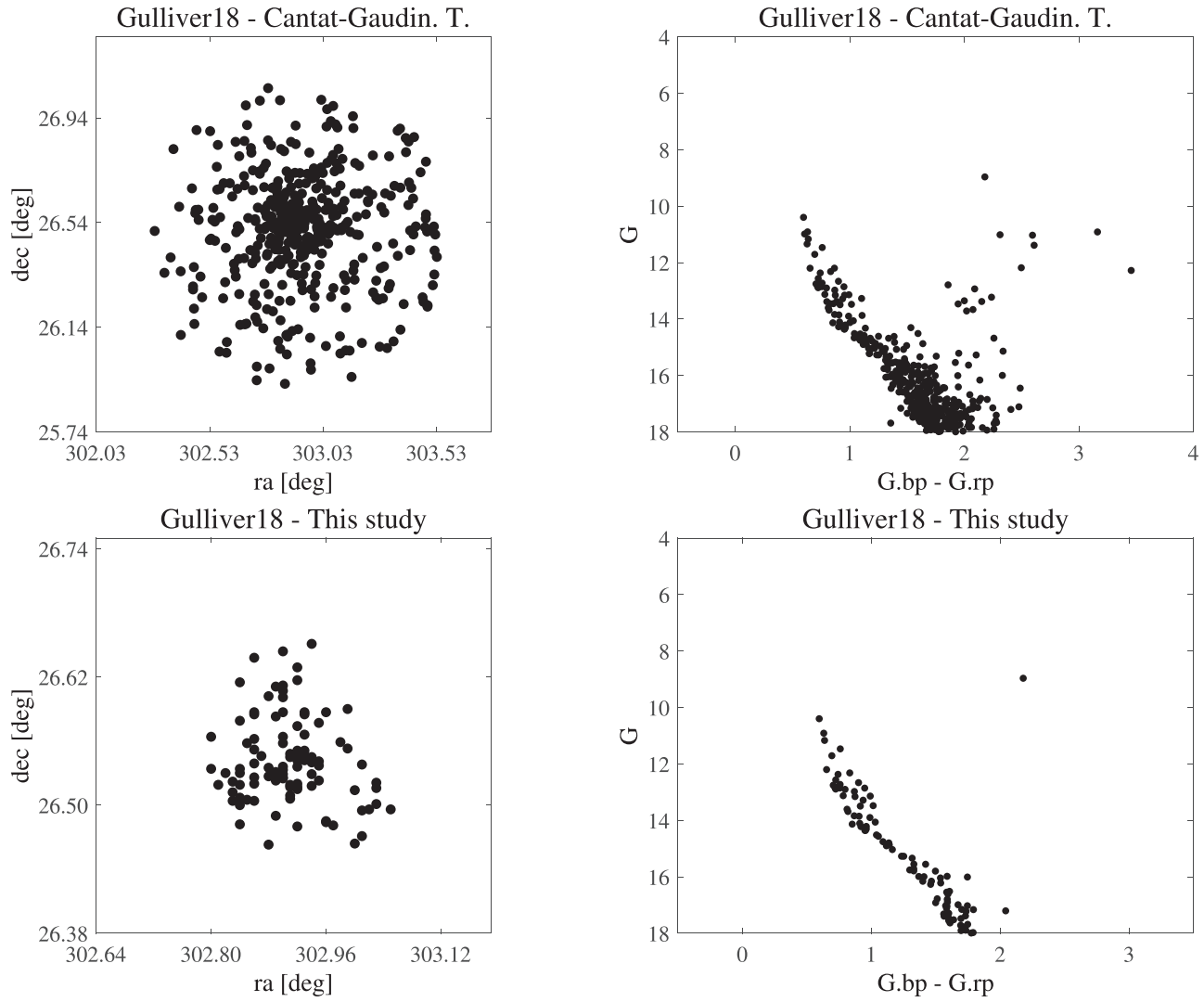

Figure 5. Top left: distribution of member stars in the sky for Gulliver18 found by Cantat-Gaudin et al. (2018a). Top right: color–magnitude diagram for Gulliver18 found by Cantat-Gaudin et al. (2018a). Bottom: the same for Gulliver18, whose member stars were found with the proposed method.

distribution in the sky and CMDs. From the figure in the top left, we can see that the distribution in the sky of member stars that were obtained by Cantat-Gaudin et al. (2018a) is extended, and its configuration is similar to a circle. Many stars were considered as memberships and the radius of the distribution approached $0\overset{\circ}{.}7$. In addition, the farther away from the center of the cluster, the more evenly distributed the member stars. Actually, we could obtain the same result in practice. This means that we could also gain abundant member stars for this candidate with approximate positions and proper motions in this small region, although we abandoned it.

What should be emphasized is that the member stars of an OC not only have a similar position and proper motion, but, more crucially, they form at almost the same time in the same giant molecular cloud. The distribution of member stars in the CMDs is almost concentrated on a theoretical curve. Obviously, the distribution in Cantat-Gaudin et al. (2018a) is not concentrated on a curve, according to the figure in the bottom left, and we cannot unveil a theoretical curve that is specific. The distribution of many member stars is exceptionally cluttered, particularly for darker stars. For comparison, we can say that the member stars we obtained are obviously concentrated on a theoretical line in the CMDs, even darker stars that are not discrete. Therefore, the member stars for the candidate we obtained have higher accuracy. We also made comparisons of the parameters for the 54 clusters in Cantat-Gaudin et al. (2018a) (Table 3).

Figure 6 shows a comparison between this study and Cantat-Gaudin et al. (2018a) of each parameter (parallax, R, D, and proper motion) for the 54 clusters. The parallax, distance, and proper motion in this study were consistent with those of the previous project. The radius of each OC that we determined

Table 3
Differences between Our Way of Determining Parameters and that of Cantat-Gaudin et al. (2018a)

Cluster	This Study					Cantat-Gaudin. T. et al.						
	ϖ (mas)	$\mu\alpha^*$ (mas yr^{-1})	$\mu\delta$ (mas yr^{-1})	R (deg)	D pc	ϖ (mas)	$\mu\alpha^*$ (mas yr^{-1})	$\mu\delta$ (mas yr^{-1})	R (deg)	D pc	$D+$ pc	$D-$ pc
Gulliver 1	0.34(0.01)	−7.83(0.05)	3.63(0.03)	0.02	2937.9(21.7)	0.32 (0.04)	−7.93(0.08)	3.58(0.08)	0.09	2837.3	2210.6	3693.2
Gulliver 2	0.68(0.01)	−4.96(0.02)	4.54(0.03)	0.02	1465.1(16.1)	0.70 (0.06)	−4.95(0.10)	4.58(0.12)	0.07	1379.2	1212.1	1600.4
Gulliver 3	0.19(0.01)	−2.93(0.03)	4.10(0.03)	0.02	5126.6(22.5)	0.19 (0.07)	−2.96(0.09)	4.11(0.11)	0.04	4550.3	3127.0	8345.1
Gulliver 4	0.30(0.01)	−2.95(0.02)	3.07(0.02)	0.03	3318.4(25.8)	0.30 (0.04)	−2.91(0.06)	3.03(0.06)	0.08	3042.1	2332.3	4372.9
Gulliver 5	0.42(0.01)	−5.03(0.02)	4.98(0.03)	0.08	2398.4(21.4)	0.41 (0.03)	−5.10(0.03)	4.90(0.07)	0.11	2297.8	1868.4	2981.3
Gulliver 6	2.37(0.01)	0.02(0.03)	−0.21(0.05)	0.12	421.1(13.9)	2.37 (0.11)	−0.01(0.39)	−0.21(0.37)	0.52	417.3	400.6	435.5
Gulliver 7	0.09(0.01)	−3.54(0.02)	3.14(0.02)	0.03	11078.7(21.2)	0.08 (0.05)	−3.55(0.15)	3.11(0.10)	0.03	8844.8	4693.3	∞
Gulliver 8	0.84(0.02)	−0.15(0.05)	−3.12(0.07)	0.06	1196.7(8.6)	0.87 (0.09)	−0.16(0.23)	−2.98(0.15)	0.10	1110.3	999.3	1249.0
Gulliver 9	1.97(0.01)	−5.79(0.05)	6.88(0.07)	0.09	507.9(22.9)	1.99 (0.09)	−5.99(0.27)	6.92(0.38)	0.97	496.5	473.0	522.4
Gulliver 10	1.62(0.02)	−4.52(0.10)	5.06(0.10)	0.11	619.5(8.3)	1.65 (0.08)	−4.44(0.24)	4.97(0.15)	0.18	594.9	561.5	632.6
Gulliver 11	1.06(0.02)	0.36(0.04)	−2.24(0.03)	0.04	941.2(19.5)	1.06 (0.07)	0.40(0.21)	−2.23(0.15)	0.13	917.3	840.2	1009.9
Gulliver 12	0.54(0.01)	−6.28(0.05)	0.16(0.05)	0.02	1857.5(67.4)	0.56 (0.03)	−5.95(0.07)	−0.41(0.09)	0.08	1699.4	1452.6	2047.4
Gulliver 13	0.63(0.01)	−2.87(0.03)	0.28(0.04)	0.03	1589.4(23.5)	0.62 (0.06)	−2.94(0.13)	0.28(0.11)	0.12	1540.4	1334.9	1820.8
Gulliver 14	0.72(0.01)	−3.68(0.05)	−4.73(0.06)	0.05	1389.5(21.3)	0.75 (0.04)	−3.72(0.07)	−4.79(0.09)	0.18	1291.5	1143.8	1483.1
Gulliver 15	0.50(0.01)	−1.06(0.03)	−1.59(0.02)	0.06	1989.8(27.6)	0.51 (0.07)	−1.06(0.12)	−1.64(0.10)	0.09	1869.3	1574.8	2299.2
Gulliver 16	0.21(0.01)	−1.26(0.01)	−0.59(0.01)	0.03	4903.7(26.4)	0.21 (0.07)	−1.25(0.06)	−0.61(0.08)	0.05	4217.7	2964.6	7288.6
Gulliver 17	0.56(0.01)	−1.11(0.02)	−3.06(0.03)	0.03	1777.2(33.3)	0.56 (0.04)	−1.08(0.12)	−3.03(0.15)	0.06	1711.8	1461.7	2065.0
Gulliver 18	0.61(0.01)	−3.18(0.02)	−5.66(0.02)	0.06	1630.2(18.1)	0.61 (0.06)	−3.20(0.09)	−5.65(0.10)	0.12	1558.6	1348.4	1846.3
Gulliver 19	0.63(0.01)	0.89(0.04)	−2.25(0.03)	0.08	1602.5(18.6)	0.63 (0.06)	0.89(0.13)	−2.26(0.15)	0.16	1507.9	1310.3	1775.7
Gulliver 20	2.36(0.02)	0.99(0.10)	−6.38(0.21)	0.15	423.3(11.9)	2.35 (0.08)	1.04(0.25)	−6.53(0.17)	0.70	420.9	403.9	439.4
Gulliver 21	1.49(0.01)	−1.95(0.05)	4.16(0.05)	0.08	672.8(15.3)	1.50 (0.05)	−1.93(0.12)	4.21(0.14)	0.36	652.2	612.3	697.8
Gulliver 22	1.28(0.02)	−1.37(0.08)	−4.62(0.10)	0.08	781.2(6.7)	1.26 (0.11)	−1.52(0.29)	−4.61(0.12)	0.12	777.8	721.7	843.4
Gulliver 23	0.25(0.01)	−2.47(0.01)	−4.44(0.01)	0.04	3912.3(20.6)	0.25 (0.05)	−2.45(0.09)	−4.44(0.10)	0.05	3643.0	2670.1	5723.3
Gulliver 24	0.64(0.01)	−3.23(0.04)	−1.52(0.03)	0.07	1563.3(16.4)	0.64 (0.05)	−3.24(0.10)	−1.57(0.09)	0.10	1504.9	1308.1	1771.6
Gulliver 25	0.75(0.02)	1.01(0.09)	−4.23(0.10)	0.10	1329.8(11.3)	0.71 (0.05)	0.96(0.11)	−4.09(0.10)	0.33	1351.3	1190.4	1562.4
Gulliver 26	0.34(0.01)	1.94(0.03)	−2.85(0.02)	0.05	3015.7(21.0)	0.36 (0.08)	2.02(0.17)	−2.87(0.13)	0.08	2570.1	2044.5	3459.1
Gulliver 27	0.32(0.01)	−4.67(0.02)	3.47(0.02)	0.03	3095.9(26.8)	0.32 (0.03)	−4.66(0.07)	3.47(0.08)	0.05	2850.4	2218.1	3987.1
Gulliver 28	1.61(0.03)	−4.21(0.18)	−3.51(0.19)	0.16	619.2(5.9)	1.58 (0.07)	−4.49(0.16)	−3.40(0.14)	0.56	621.3	584.9	662.5
Gulliver 29	0.91(0.01)	1.24(0.04)	−2.12(0.04)	0.03	1090.4(29.6)	0.91 (0.06)	1.33(0.16)	−2.21(0.17)	0.68	1070.9	967.3	1199.3
Gulliver 30	0.44(0.01)	−2.48(0.03)	−3.72(0.02)	0.03	2269.8(24.5)	0.43 (0.04)	−2.52(0.07)	−3.70(0.07)	0.08	2192.3	1797.7	2808.6
Gulliver 31	0.37(0.01)	−1.50(0.03)	−3.12(0.03)	0.02	2724.6(26.8)	0.40 (0.03)	−1.50(0.06)	−3.11(0.09)	0.08	2352.8	1905.6	3077.1
Gulliver 32	0.57(0.01)	−0.98(0.04)	2.35(0.07)	0.03	1751.7(34.5)	0.58 (0.06)	−0.88(0.10)	2.30(0.11)	0.10	1469.8	1416.2	1975.6
Gulliver 33	0.84(0.01)	0.25(0.05)	−3.81(0.08)	0.09	1193.3(12.4)	0.87 (0.06)	0.27(0.12)	−3.96(0.07)	0.31	1116.5	1044.6	1256.9
Gulliver 34	0.22(0.01)	−6.27(0.03)	2.42(0.02)	0.05	4641.0(61.2)	0.22 (0.03)	−6.18(0.06)	2.41(0.07)	0.05	3972.3	2842.1	6580.6
Gulliver 35	0.24(0.01)	−3.90(0.03)	−6.09(0.04)	0.02	4207.1(21.0)	0.23 (0.07)	−3.91(0.14)	−6.26(0.16)	0.06	3906.2	2808.8	6406.3
Gulliver 36	0.74(0.01)	−0.21(0.03)	0.61(0.04)	0.02	1343.3(30.6)	0.73 (0.04)	−0.24(0.08)	0.61(0.07)	0.40	1326.7	1171.3	1529.6
Gulliver 37	0.64(0.01)	−0.78(0.04)	−3.70(0.04)	0.06	1560.1(16.6)	0.64 (0.04)	−0.78(0.07)	−3.74(0.09)	0.11	1490.9	1297.6	1751.8
Gulliver 38	0.40(0.01)	−0.95(0.01)	−2.57(0.02)	0.03	2477.5(24.6)	0.40 (0.04)	−0.92(0.12)	−2.59(0.13)	0.06	2329.1	1889.9	3036.6
Gulliver 39	0.34(0.01)	−4.43(0.02)	1.28(0.02)	0.03	2982.4(28.1)	0.34 (0.04)	−4.41(0.07)	1.27(0.06)	0.05	2747.5	2155.3	3788.6
Gulliver 40	0.58(0.01)	−7.67(0.07)	2.61(0.06)	0.06	1732.3(19.9)	0.59 (0.04)	−7.69(0.04)	2.48(0.06)	0.08	1618.7	1393.1	1931.3
Gulliver 41	0.17(0.01)	−1.79(0.10)	−4.04(0.06)	0.04	4970.7(27.9)	0.17 (0.13)	−1.79(0.30)	−4.71(0.26)	0.03	5000.2	3333.8	9982.9
Gulliver 42	0.18(0.01)	−2.63(0.03)	−5.51(0.03)	0.02	5684.2(21.3)	0.18 (0.17)	−2.78(0.19)	−5.45(0.22)	0.05	4763.9	3226.7	9092.1
Gulliver 43	0.34(0.01)	−2.92(0.02)	−5.75(0.02)	0.05	2929.0(29.8)	0.35 (0.05)	−2.92(0.09)	−5.80(0.10)	0.08	2631.6	2083.3	3571.7
Gulliver 44	0.79(0.01)	−0.66(0.02)	2.33(0.03)	0.07	1268.8(23.1)	0.79 (0.05)	−0.67(0.14)	2.30(0.13)	0.19	1228.2	1093.9	1400.2
Gulliver 45	0.27(0.01)	−0.76(0.03)	2.43(0.03)	0.03	3648.8(20.8)	0.28 (0.09)	−0.76(0.20)	2.51(0.19)	0.05	3196.9	2422.4	4699.2
Gulliver 46	0.18(0.01)	−6.90(0.02)	0.13(0.01)	0.03	5367.8(21.7)	0.18 (0.06)	−6.95(0.09)	0.13(0.07)	0.02	4766.3	3227.8	9113.6

Table 3
(Continued)

Cluster	This Study					Cantat-Gaudin. T. et al.						
	ϖ (mas)	$\mu\alpha^*$ (mas yr^{-1})	$\mu\delta$ (mas yr^{-1})	R (deg)	D pc	ϖ (mas)	$\mu\alpha^*$ (mas yr^{-1})	$\mu\delta$ (mas yr^{-1})	R (deg)	D pc	$D+$ pc	$D-$ pc
Gulliver 47	0.39(0.01)	0.32(0.04)	−2.61(0.03)	0.06	2512.8(34.8)	0.37 (0.05)	0.33(0.15)	−2.54(0.11)	0.12	2539.0	2024.9	3403.0
Gulliver 48	1.06(0.01)	−4.70(0.06)	−6.77(0.06)	0.08	938.5(15.6)	1.06 (0.05)	−4.78(0.14)	−6.67(0.17)	0.28	919.8	842.3	1013.0
Gulliver 49	0.58(0.02)	−3.99(0.02)	−3.05(0.02)	0.09	1721.0(21.3)	0.59 (0.04)	−4.02(0.11)	−3.05(0.11)	0.16	1621.7	1395.5	1936.5
Gulliver 50	0.51(0.01)	−7.24(0.02)	1.68(0.01)	0.02	1971.7(38.4)	0.51 (0.04)	−7.20(0.10)	1.66(0.06)	0.11	1841.7	1554.9	2256.8
Gulliver 51	0.65(0.01)	−4.89(0.04)	−0.09(0.03)	0.03	1539.7(21.1)	0.65 (0.03)	−4.89(0.10)	−0.15(0.08)	0.08	1479.6	1288.9	1736.5
Gulliver 52	0.40(0.01)	−4.77(0.02)	1.46(0.02)	0.02	2462.6(49.8)	0.40 (0.04)	−4.76(0.07)	1.47(0.08)	0.15	2350.8	1903.3	3073.5
Gulliver 53	0.36(0.01)	0.48(0.04)	−2.89(0.02)	0.07	2780.0(26.6)	0.38 (0.04)	0.40(0.11)	−2.84(0.11)	0.12	2421.9	1949.5	3196.2
Gulliver 54	0.78(0.02)	−0.57(0.05)	−7.23(0.06)	0.06	1279.4(15.6)	0.79 (0.06)	−0.60(0.14)	−7.30(0.18)	0.10	1219.0	1086.5	1388.3

Note. The parameters shown are the mean and standard deviation of these 54 known objects in this study (left). Parameters come from Cantat-Gaudin et al. (2018a) (right).

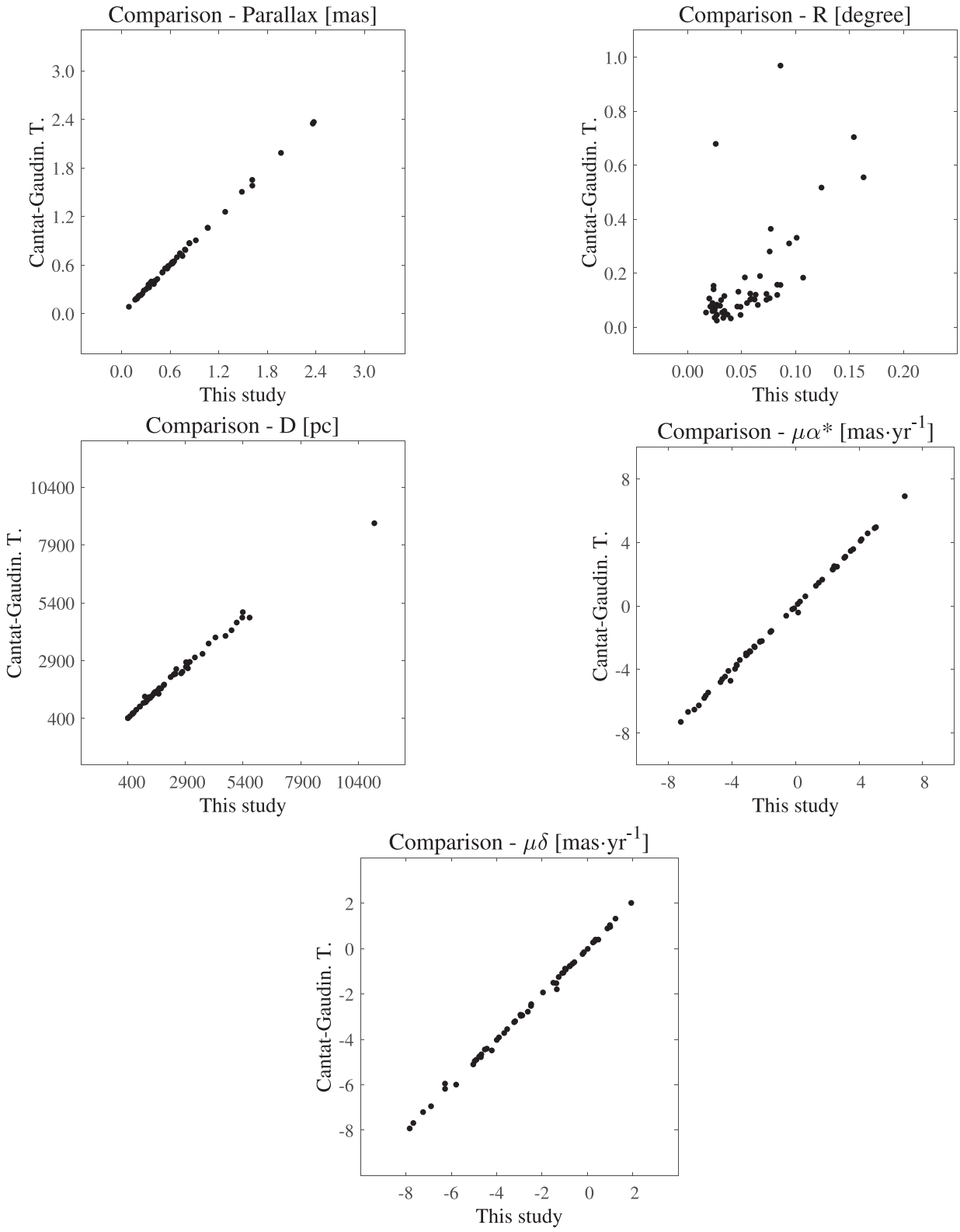

Figure 6. Comparison of our study to that of Cantat-Gaudin et al. (2018a) in terms of the five parameters (parallax, R, D, and proper motions) for the 54 clusters.

was smaller than before, at approximately $1/4$ of the value given by Cantat-Gaudin et al. (2018a). This indicates that the distribution of member stars we obtained is more concentrated, and it can be considered that the memberships are more credible. Particularly, the radius of Gulliver9 and Gulliver20 is much smaller. These two objects are closer. In fact, we obtained more memberships when the tiles were slightly larger. Considering the projection effect of the spatial distribution of the targets, the distribution scales of OCs at different distances are dissimilar. The closer the OC is, the larger the scale is. And the scale is smaller when the target is farther away. Therefore, we believe that we can find more OCs by changing the distance resolution.

We confirmed 54 OC candidates discovered with the proposed SBCSM. Among these, 16 OC candidates were newly discovered. These new candidates may have been omitted due to defects in previous methods, such as excessive sample space or unreasonable parameter selection. This shows that our method outperforms previous methods, and that there are still many OCs that have not yet been detected. Moreover, the confirmation of the memberships of OCs is a problem that remains to be solved. In addition, *Gaia* contains radial velocities for 7 million stars, which we did not employ in this study. However, these radial velocities will facilitate the study of OCs, and, particularly, research on galactic kinematics. Similarly, OCs serve as excellent tracers for the study of the mechanism of star formation and the structure of the Milky Way.

6. Summary

We proposed a novel method, called SBCSM, which makes full use of the astrometric parameters and three-band photometry released by *Gaia* DR2 to detect new OCs in the Milky Way. The SBCSM offers high spatial resolution, and the memberships it obtains have higher accuracy. Starting from a sample of 54 OC candidates found by Cantat-Gaudin et al. (2018a), our proposed SBCSM detected 104 other objects. Among these, 16 OC candidates were newly discovered. Owing to the projection effect of the spatial distribution of the OCs, future methods should consider the effect of distance.

The astrometric parameters for these 16 new OC candidates were presented, including their age. This work challenges previous claims that the census of OCs is complete up to distances of 1.8 kpc. With more sources and fewer errors in the *Gaia* data, more OCs can be discovered.

This work was funded by the NSFC, grant numbers 11933011, 11873019, and 11673066, and by the Key Laboratory for Radio Astronomy.

Appendix
Maps, Proper Motions, and CMDs for 16 New Candidates

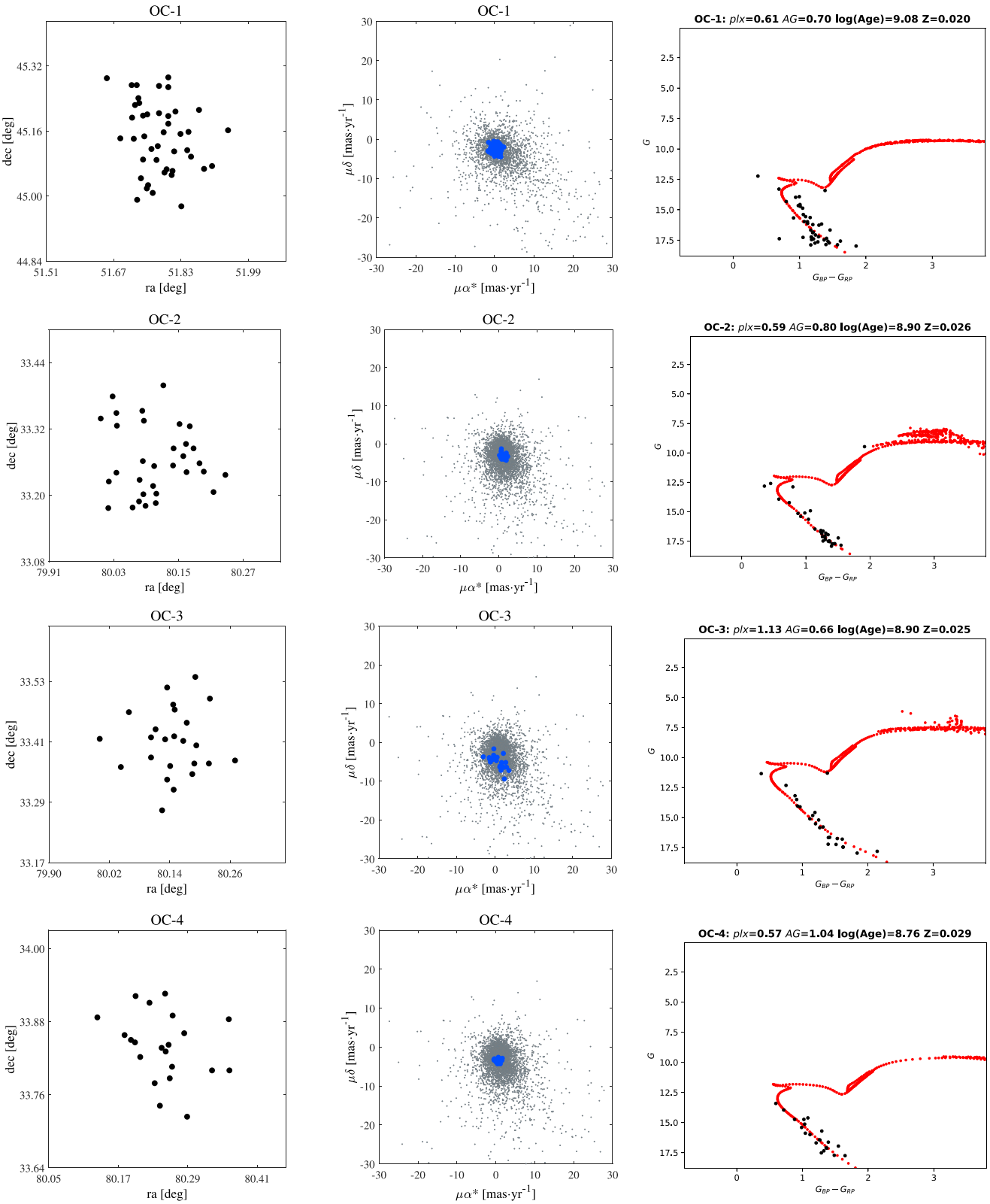

Figure 7. Maps (left) and proper motion (middle): member stars (blue) together with field stars (gray), and CMDs (the red curves are theoretical isochrones) for new OC candidates (left).

(A color version of this figure is available in the online journal.)

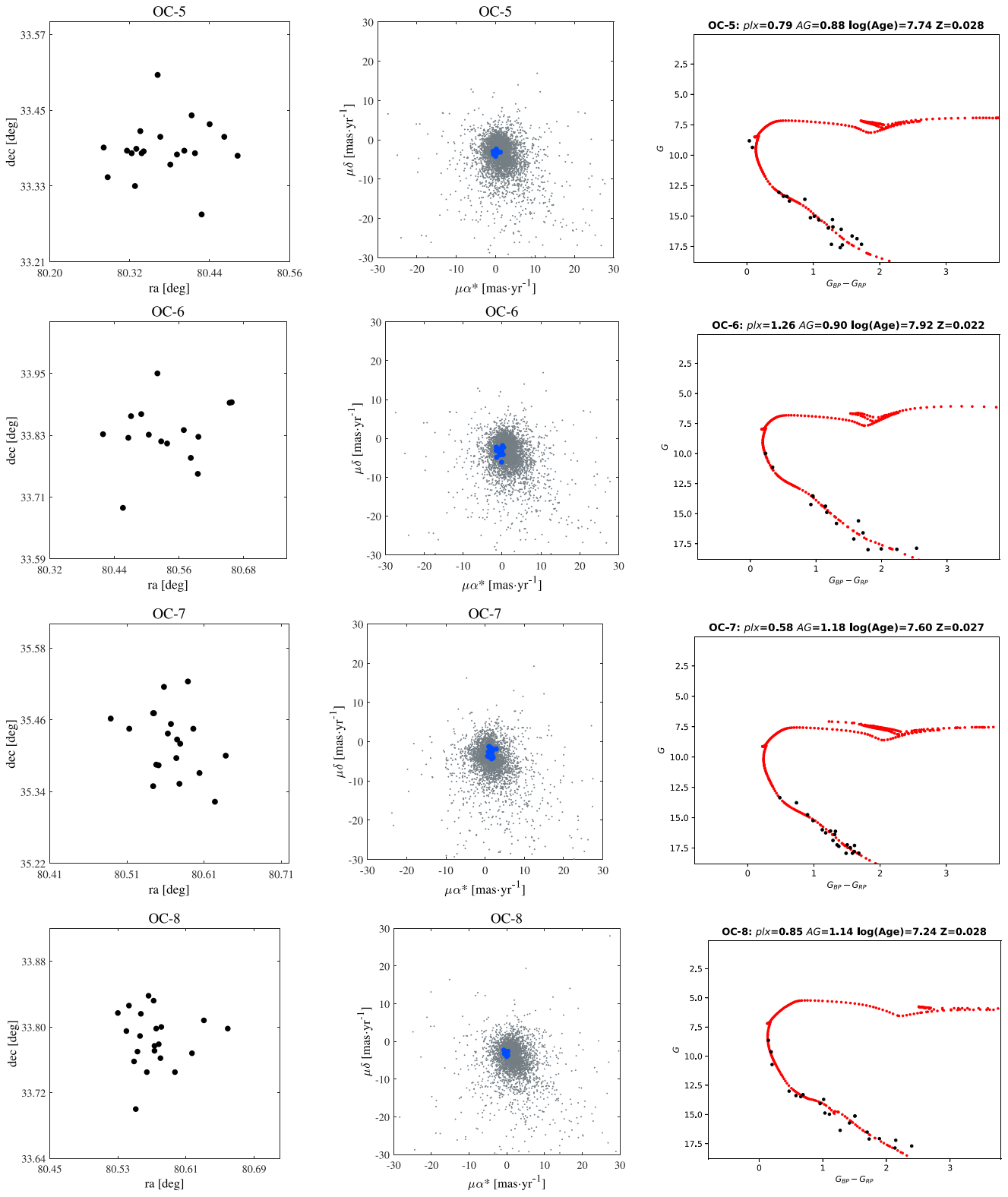

Figure 7. (Continued.)

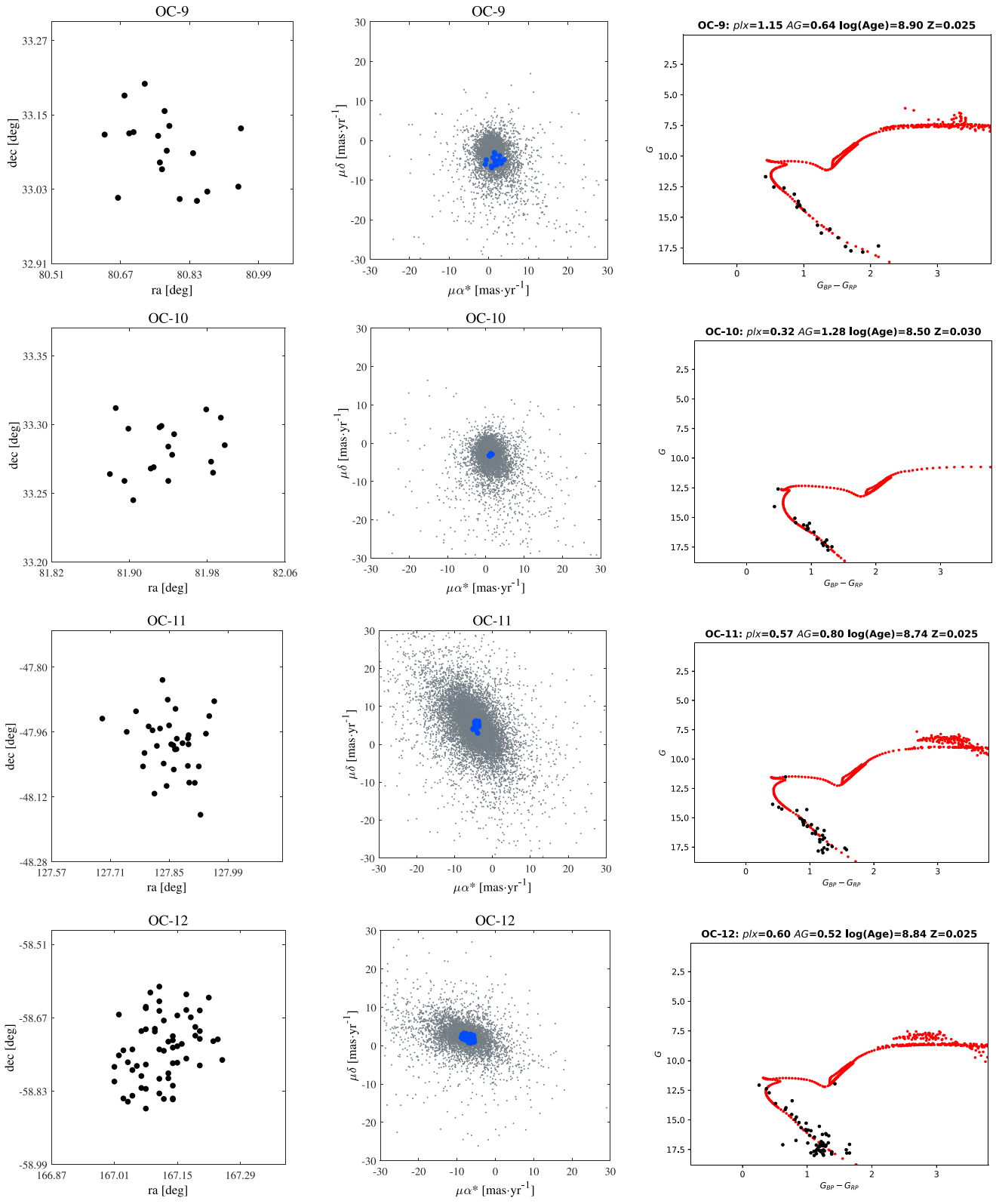

Figure 7. (Continued.)

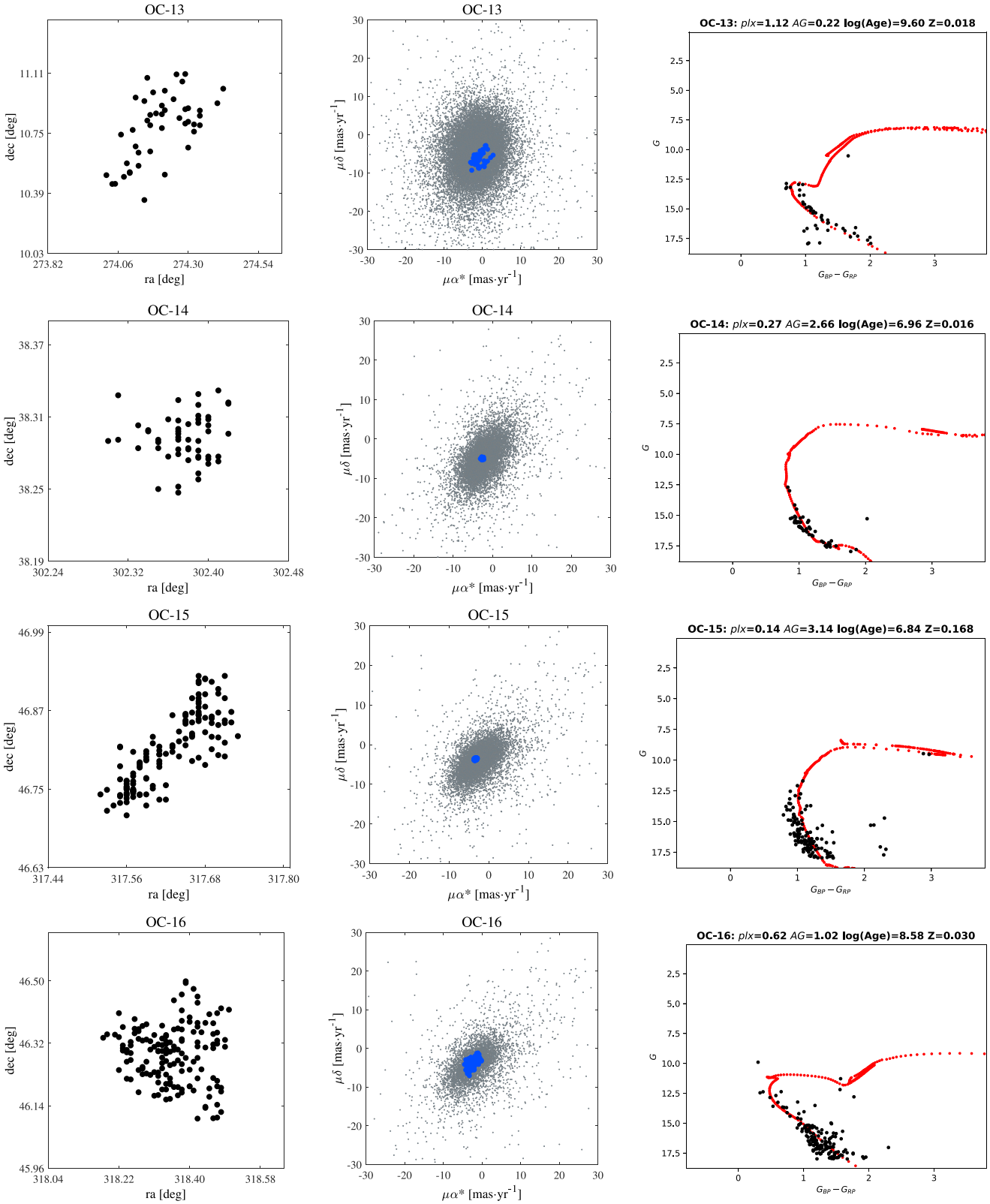

Figure 7. (Continued.)

References

Alessi, B. S., Moitinho, A., & Dias, W. S. 2003, A&A, 410, 565
Altman, N. S. 1992, BAN, 46, 175
Bressan, A., Marigo, P., Girardi, L., et al. 2012, MNRAS, 427, 127
Cantat-Gaudin, T., Jordi, C., Vallenari, A., et al. 2018a, A&A, 618, A93
Cantat-Gaudin, T., Krone-Martins, A., et al. 2018b, A&A, 624, A126
Cardelli, J. A., Clayton, G. C., & Mathis, J. S. 1989, ApJ, 345, 245
Castro-Ginard, A., Jordi, C., Luri, X., et al. 2018, A&A, 618, A59
Castro-Ginard, A., Jordi, C., Luri, X., et al. 2019, A&A, 627, A35
Dias, W. S., Alessi, B. S., Moitinho, A., & Lépine, J. R. D. 2002, A&A, 389, 871
Dias, W. S., & Lépine, J. R. D. 2005, ApJ, 629, 825
Dias, W. S., Monteiro, H., Caetano, T. C., et al. 2014, A&A, 564, A79
Ester, M., Kriegel, H.-P., Sander, J., & Xu, X. 1996, VA, 41, 397
Evans, D., Riello, M., De Angeli, F., et al. 2018, A&A, 616, A4
Froebrich, D., Scholz, A., & Raftery, C. L. 2007, MNRAS, 374, 399
Gaia Collaboration, Brown, A. G. A., Vallenari, A., et al. 2018, A&A, 616, A1
Janes, K., & Adler, D. 1982, ApJS, 49, 425
Kemal, V., & Yakup, A. 2018, DSL, 7, 119
Kharchenko, N. V., Piskunov, A. E., Röser, S., Schilbach, E., & Scholz, R.-D. 2005, A&A, 440, 403
Kharchenko, N. V., Piskunov, A. E., Schilbach, E., Röser, S., & Scholz, R.-D. 2013, A&A, 558, A53
Krone-Martins, A., & Moitinho, A. 2014, A&A, 561, A57
Lada, E. A., Strom, K. M., & Myers, P. C. 1993, in Protostars and Planets III, ed. E. H. Levy & J. I. Lunine (Tucson, AZ: Univ. Arizona Press), 245
Lampe, O. D., & Hauser, H. 2011, 2011 IEEE Pacific Visualization Symp. (Piscataway, NJ: IEEE), 171
Lindegren, L., Lammers, U., Bastian, U., et al. 2016, A&A, 595, A4
Liu, L., & Pang, X. 2019, ApJS, 245, 32
Michalik, D., Lindegren, L., & Hobbs, D. 2015, A&A, 574, A115
Moitinho, A. 2010, in IAU Symp. 266, ed. R. de Grijs & J. R. D. Lépine (Cambridge: Cambridge Univ. Press), 106
O'Donnell, J. E. 1994, ApJ, 422, 158
Payne-Gaposchkin, C. 1979, Stars and Clusters (Camridge, MA: Harvard Univ. Press)
Piskunov, A. E., Kharchenko, N. V., Röser, S., Schilbach, E., & Scholz, R.-D. 2006, A&A, 445, 545
Röser, S., Schilbach, E., & Goldman, B. 2016, A&A, 595, A22
Schmeja, S., Kharchenko, N. V., Piskunov, A. E., et al. 2014, A&A, 568, A51
Scholz, R.-D., Kharchenko, N. V., Piskunov, A. E., Röser, S., & Schilbach, E. 2015, A&A, 581, A39
Sim, G., Lee, S. H., Ann, H. B., & Kim, S. 2019, JKAS, 52, 145
Zambom, A. Z., & Dias, R. 1998, arXiv:1212.2812